Research Square

Preprints are preliminary reports that have not undergone peer review.
They should not be considered conclusive, used to inform clinical practice,
or referenced by the media as validated information.

The Haptic Cycling Trainer (HaCT): a robotic device for lower-limb rehabilitation

Murat Sahin
University College Dublin
Andrea Ortiz-Cuadros
University College Dublin
Bahram Tarvirdizadeh
University of Tehran
Giacomo Severini
giacomo.severini@ucd.ie
University College Dublin
Donal Holland
University College Dublin

Research Article

Keywords: Bees algorithm, Cycle ergometer, Haptic interface, Rehabilitation engineering, System identification

Posted Date: April 16th, 2026

DOI: https://doi.org/10.21203/rs.3.rs-9105541/v2

License: This work is licensed under a Creative Commons Attribution 4.0 International License. Read Full License

Additional Declarations: The authors declare no competing interests.

The Haptic Cycling Trainer (HaCT): a robotic device for lower-limb rehabilitation

Murat Sahin[1], Andrea Ortiz-Cuadros[1,2], Bahram Tarvirdizadeh[1,3], Giacomo Severini[1], Dónal Holland[2]

[1]School of Electrical and Electronic Engineering, University College Dublin, Ireland

[2]School of Mechanical and Materials Engineering, University College Dublin, Ireland

[3]Faculty of New Sciences and Technology, University of Tehran, Iran

Corresponding author: Giacomo Severini (giacomo.severini@ucd.ie)

Funding statement: This work was supported by Research Ireland under Grant 12/RC/2289_P2 and Grant 21/FFP-P/10228, and by Enterprise Ireland under Grant CF/2017/0766/P.

The Haptic Cycling Trainer (HaCT): a robotic device for lower-limb rehabilitation

Abstract: This article presents a robotic rehabilitation device comprising a cycle ergometer that can guide a user's feet through non-circular trajectories while dynamically assisting or resisting motion. The device possesses three degrees of freedom: a central motor governs crank rotation, while two additional motors independently control each crank's effective length; three rotational encoders provide position feedback. Each motor is regulated by nested position (outer), velocity, and current (inner) control loops. Controller gains for each cascade stage were optimized through simulations employing a model of the physical system. Inertial and dissipative parameters within this model were estimated via system identification, wherein a population-based search algorithm minimized the discrepancy between the model's predictions and the system's measured response. Validation of both the system model and its derived controller proceeded in two stages: first examining each degree of freedom in isolation, then considering them simultaneously. Evaluation entailed comparing the physical system's response to commanded trajectories and further assessing model fidelity by contrasting simulated predictions against experimentally observed response.

Keywords: Bees algorithm, Cycle ergometer, Haptic interface, Rehabilitation engineering, System identification.

1 Introduction

Stroke is a major contributor to long-term disability worldwide, with a substantial proportion of survivors experiencing persistent functional impairment [1]. Lower limb impairment is one of the most prevalent motor deficits following stroke, frequently resulting in reduced mobility and compromised gait function [2, 3]. These impairments persist in a significant proportion of stroke survivors, limiting community ambulation and increasing long-term dependence on assistive interventions [4, 5]. Robotic-assisted gait training has been introduced to enhance repetitive, task-specific lower limb rehabilitation after stroke, aiming to improve walking function through high-intensity, controlled movement patterns [6]. Several devices, based on exoskeletal or end-effector designs, have been introduced in stroke rehabilitation to provide consistent kinematic guidance, reducing therapist burden while enabling longer training durations [7-9]. Clinical evidence indicates that electromechanical-assisted gait training combined with physiotherapy increases the likelihood of regaining independent walking in stroke survivors, particularly in the subacute phase [10]. Robotic systems have the potential to be used for facilitating lower limb therapy early after neurological injury. Early initiation of rehabilitation after stroke is critical, as the first weeks post-injury represent a heightened period of neuroplastic potential during which the brain is more responsive to motor relearning stimuli [11].

Cycling-based rehabilitation is often used as a training modality that can be employed early in the acute post-stroke phase as it promotes motor relearning and cardiovascular conditioning in a controlled manner [12]. Technology for cycling rehabilitation includes instrumented ergometers and robotic systems that enable controlled, phase-specific loading of the lower limbs. Early variable-resistance cycle ergometers allowed adjustment of mechanical load during recumbent exercise [13]. Isokinetic eccentric cycle ergometers have been developed to provide controlled eccentric muscle actions [14]. Semi-recumbent eccentric systems have been instrumented to isolate muscle contractions to specific phases of the pedal cycle, enabling targeted neuromuscular training [15, 16]. Recently, a lower-limb haptic rehabilitation robot has been designed and experimentally validated to deliver controlled force patterns during lower-extremity training [17].

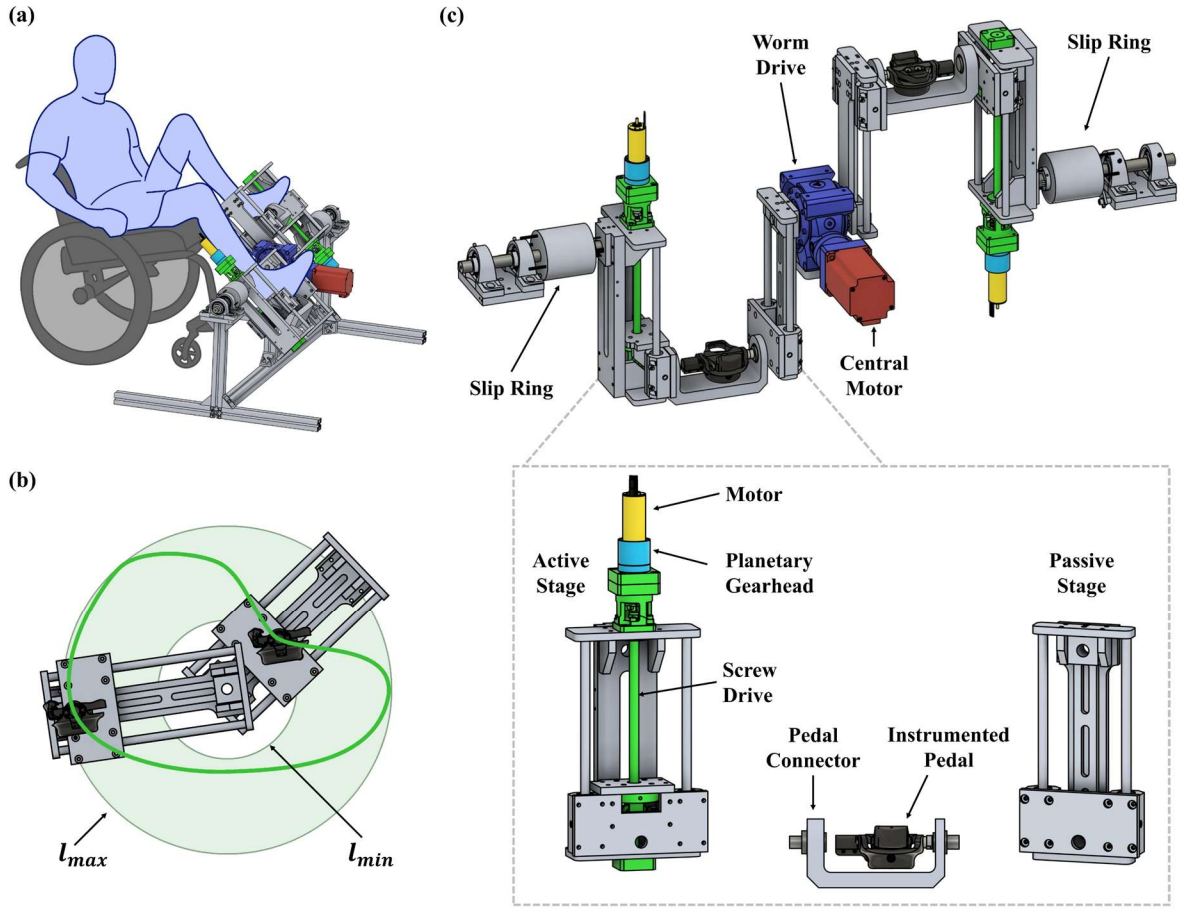


Figure 1. Mechanical design of the HaCT. **(a)** Intended use case, in which a subject pedals the device while seated in a wheelchair. **(b)** The shaded region, bounded by circles with radii equal to the maximum and minimum crank lengths, illustrates the reachable workspace for each pedal. An example trajectory is shown (thick line). **(c)** A central motor and worm drive rotates the cranks. Each crank assembly consists of an active linear stage which determines the crank length, a passive linear stage, and a pedal connector that couples the stages together (inset). To minimize the lateral distance between the pedals, the slip rings and active stages are located external to the pedals.

In this paper we present the Haptic Cycling Trainer (HaCT), a novel robotic device for cycling training that combines the repetitive, task specific nature of cycle ergometry with programmable assistance, resistance, and foot-trajectory modulation typically seen in robotic-assisted gait rehabilitation. The HaCT system is an electromechanical cycling system that can provide assistance or resistance to the user dynamically during the cycle, while follow programmable non-circular foot trajectories. The paper first describes the electromechanical design and control architecture of the HaCT system, followed by the state-space equations that were used to model the system and the system identification procedures utilized to estimate the parameters of these equations. We present the results of preliminary testing on the resulting controller, showing that the model can accurately predict the system performance, and that the HaCT device satisfies the proposed design specifications.

2 Methods

2.1 Electromechanical Design

The Haptic Cycling Trainer (HaCT, Fig.1) is a static cycle ergometer. The system has no integrated seat so that, for example, it can be used while seated in a wheelchair. The frame of the system is composed of 40x40mm aluminium T-slot extrusion, and includes a safety cage (not pictured) to keep the user's hands away from any trap or pinch risks. A single central brushless DC motor (DB80L048030-ENM05J,

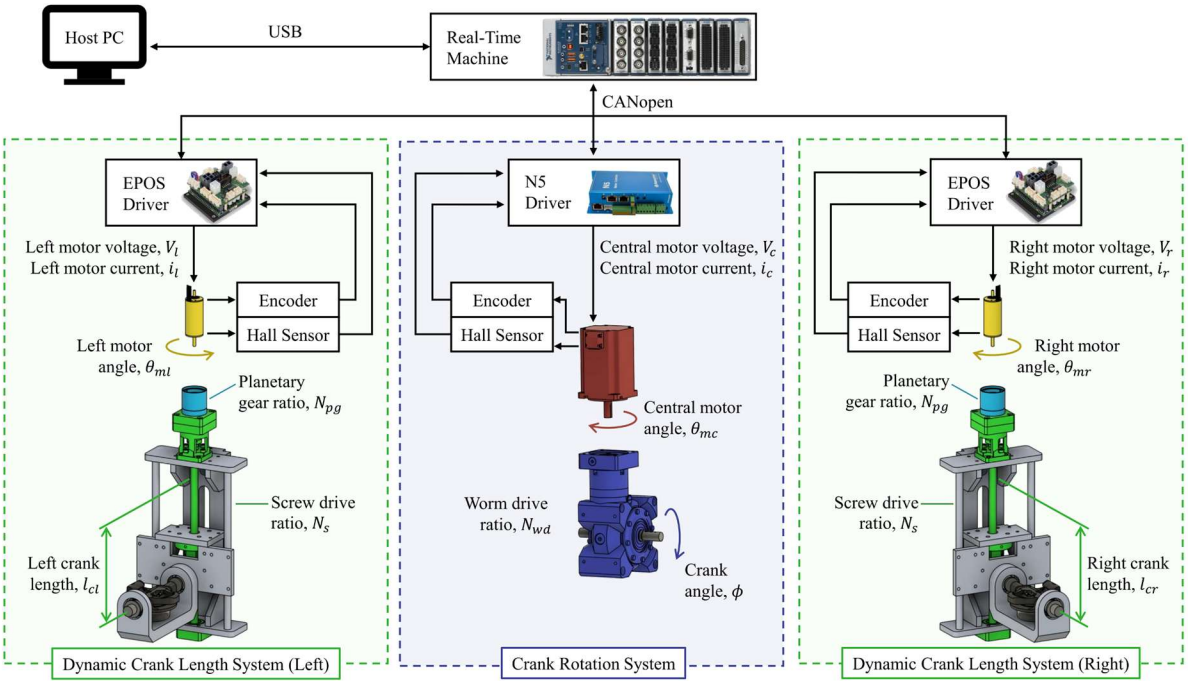


Figure 2. HaCT hardware and device architecture, with variables that will be used in the system model labelled.

Nanotec Electronic, Feldkirchen, Germany) controls the rotation of both cranks, which are coupled together such that the angle between the two cranks is always 180°, as in a standard push bicycle. A worm drive transmission with 50:1 speed reduction (VH+ 040, Wittenstein, Igersheim, Germany) reduces the rotational speed while increasing the torque transmitted from the motor, and ensures that the system cannot be back-driven. The cranks turn on three colinear mild steel shafts. The effective length of each crank can be varied independently while the cranks rotate, such that each pedal can follow an arbitrary non-circular trajectory. Each crank contains a custom linear actuator, comprising a brushless DC motor (EC-4pole 30-305013, Maxon Group, Sachseln, Switzerland), a planetary gearhead with a reduction of 4.3:1 (GP 42 C, Maxon, Sachseln, Switzerland), and a ball screw drive with a screw lead of 12.7 mm (PowerTrac SRT 0500-0500 RH, Nook Industries, Cleveland, Ohio). Custom carriages incorporating ball bearings (TTGE-12-SPMWW, THN, Enschede, The Netherlands) slide on precision-machined hardened steel cylindrical guides. With the exception of the steel shafts and guides, all custom parts are composed of aluminium. Each crank's length can vary between 100 mm and 240 mm. In comparison, standard push bicycle cranks have a length of 170 mm.

The form factor of HaCT is dictated by a requirement to keep the lateral distance between the two pedals to a minimum; too large a lateral distance would require an excessive amount of hip abduction for the user, which would be uncomfortable and would interfere with the intended use of the device. The motors that control the crank lengths rotate along with the cranks, and therefore require the transmission of power and signals via slip rings that occupy substantial lateral space. These motors and the associated transmissions add to the space required. The system's design places these components external to the user's legs, with lower-profile passive linear stages located medial to the user's legs. The active and passive linear stages are connected via a custom pedal connector part, such that, for each leg, a single motor controls the length of both stages.

In addition to Hall Effect sensors in each motor, the system's sensors include three rotational encoders (Fig. 2). The central motor's position is monitored using a magnetic incremental encoder with a resolution of 4096 counts per revolution (NME-1, Nanotec Electronic, Feldkirchen, Germany). The crank length motors incorporate incremental encoders with a resolution of 1024 counts per revolution (ENC 16 EASY, Maxon Group, Sachseln, Switzerland). User interactions with the system are measured

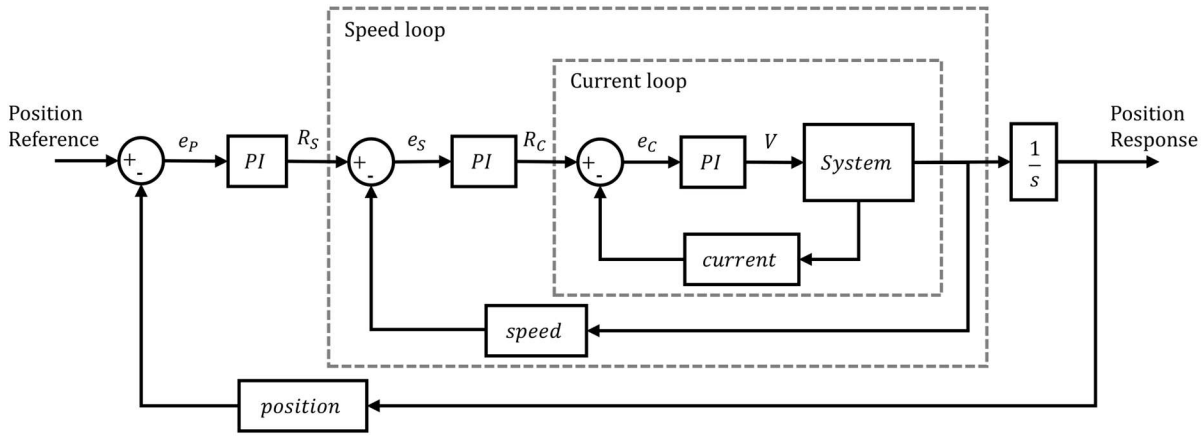


Figure 3. Control architecture for each subsystem in HaCT, where e_P, e_S, and e_C are the position, speed, and current errors respectively; R_S and R_C are the speed and current references respectively, and V is the resulting voltage applied to the system by the controller.

via two instrumented pedals (I-CrankSet ICS-RM, Sensix, Poitiers France), each of which contains a 6-axis force/torque sensor and an additional encoder. This article does not consider user interactions, so data from these sensors will not be considered here.

A CompactRIO-based controller (NI 9047, National Instruments, Austin, TX, USA) manages the system through a CANopen network. CANopen communication is handled by an interface card (NI 9881, National Instruments, Austin, TX, USA) installed on the CompactRIO. The first node on the CANopen bus is the central motor driver (N5 CANopen, Nanotec, Feldkirchen, Germany), which operates using pulse-width modulation (PWM). The remaining nodes are the crank length motor drivers (Epos 4, Maxon, Sachseln, Switzerland), which are similarly controlled via PWM. CompactRIO's real-time environment generates the required speed commands and transmits them to the drivers via CANopen. Feedback signals from the drivers are used to update the control algorithm.

Safety features include a physical emergency stop button for rapid power shutdown. The control software limits the central motor speed to 1,500 rpm, corresponding to a crank rotation of 30 rpm. While unimpaired cycling typically involves crank rotation of approximately 60 rpm, a lower speed limit was selected as appropriate for the intended rehabilitation application. The crank motor speed is restricted to 1,290 rpm, corresponding to a screw drive output speed of 0.6 m/s. The software verifies the trajectory validity before each test, preventing initiation if parameters are unsuitable. An emergency stop routine runs in parallel with the main control loop, allowing immediate test termination upon activation of a software interface stop button.

2.2 Software and Control Architecture

The real-time control software was developed in LabVIEW 2019 (National Instruments, Austin, TX, USA) using a state machine architecture to accommodate the sequential operations required for CANopen communication. The primary control loop executes every 10 ms. During operation, motor position, speed, and current data are streamed to the user interface via Network Streams to ensure lossless data transfer.

For each of the three mechatronic subsystems depicted in Fig. 2, the control architecture consists of a three-level cascade control scheme, comprising nested position, speed, and current loops that allow for independent regulation (Fig. 3). The primary advantage of this tiered structure is its ability to isolate and suppress disturbances locally, preventing their propagation through the broader system [18]. Specifically, by managing current dynamics within the innermost loop, the system can mitigate transient spikes during abrupt position commands, thereby ensuring electrical safety and smoother motion

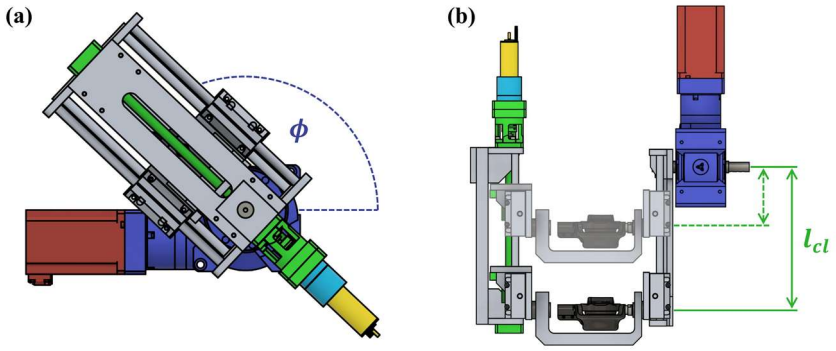


Figure 4. (a) The crank angle is defined as the angle between the left crank and horizontal. **(b)** Illustration of the moving mass associated with changes in the crank length.

profiles. The outer levels manage speed and position control, integrated with optical encoder feedback to ensure spatial accuracy [19].

Such nested control systems require the separation of bandwidths. To facilitate stability and decouple the dynamics of each layer, the inner loops are designed to operate at a frequency at least four to five times higher than their immediate outer counterparts [20]. This frequency separation ensures that the inner loop reaches a steady state before the outer loop significantly changes its command signal. For the crank rotation system, a bandwidth of 2 Hz, which is approximately equal to the voluntary force control bandwidth of the human leg [21], was chosen as an appropriate target for the position loop; design specifications of 10 Hz for the speed loop and 50 Hz for the current loop were defined based on this. For the dynamic crank length system, the design specifications were empirically defined as 4 Hz for the position loop, 20 Hz for the velocity loop, and 100 Hz for the current loop. To eliminate steady-state error across all loops, a Proportional-Integral (PI) control law is applied to each layer.

In order to tune the PI controllers and achieve the target bandwidths, an accurate model of the system is required. While the fundamental mathematical models for the motors, gears, and screws are well-defined, the structural complexity of the HaCT system introduces uncertainties regarding the effective inertia and friction in each subsystem. The following section describes state-space models that were derived to describe each subsystem.

2.3 State-Space Model

As illustrated in Fig. 2, HaCT consists of three mechatronic subsystems: the crank rotation system and the left and right dynamic crank length systems. In the modelling that follows, the subscripts *c*, *l*, and *r* are used to refer to each of these subsystems respectively. The left and right dynamic crank systems are assumed to be identical; only the model for the left crank is presented here. Each subsystem was represented with a state-space model in the form

$$\dot{x} = \frac{d}{dt}\begin{bmatrix}\theta_m \\ \dot{\theta}_m \\ i\end{bmatrix} \tag{1}$$

$$y = \begin{bmatrix}1 & 0 & 0\end{bmatrix}\begin{bmatrix}\theta_m \\ \dot{\theta}_m \\ i\end{bmatrix} \tag{2}$$

where θ_m is the position of the motor and i is the armature current. Assuming the commutation algorithm is done correctly and is fast enough, the electrical dynamics of the BLDC motors can be represented by the brushed DC motor model:

$$\frac{di}{dt} = \frac{1}{L}\left(V - Ri - K_e\dot{\theta}_m\right) \tag{3}$$

where L is the armature inductance, V is the applied armature voltage, R is the armature resistance, and K_e is the motor back EMF constant.

The general form of the mechanical dynamics model is

$$K_t i = J_{eq}\ddot{\theta}_m + b_{eq}\dot{\theta}_m + \tau_l \tag{4}$$

where K_t is the motor torque constant, J_{eq} is the equivalent inertia or the total effective inertia reflected to the motor shaft, b_{eq} is the equivalent viscous damping coefficient, and τ_l is the external load torque reflected to the motor shaft.

The mechanical dynamics for the crank rotation system, referred to here with the subscript c, are modelled as

$$\frac{d}{dt}\dot{\theta}_{mc} = \frac{1}{J_{eqc}}\left(K_{tc}i_c - b_{eqc}\dot{\theta}_{mc} - \frac{1}{N_w}\tau_{gc}\right) \tag{5}$$

where N_w is the transmission ratio of the worm drive, and τ_{gc} is a load torque due to gravity. For standard cycle ergometers, where both cranks have the same length and mass, the weight of the cranks balance each other and there is no net torque due to gravity. In contrast, each of the HaCT system's cranks can change length independently, so this balancing cannot be assumed. The gravity torque is modelled as

$$\tau_{gc} = m_p g(l_{cr} - l_{cl})\cos(\phi) \tag{6}$$

where m_p is the mass of the pedal assembly, that is the mass of the components that move to change the crank length, g is the acceleration due to gravity, l_{cr} and l_{cl} are the effective lengths of the right and left cranks respectively, and ϕ is the angle that the left crank makes with horizontal (see Fig. 4). The distribution of mass around the crank axis of rotation varies as the crank lengths change, so the equivalent inertia is a function of the right and left crank lengths in the form:

$$J_{eqc} = A\left(l_{cr}^2 + l_{cl}^2\right) + B(l_{cr} + l_{cl}) + C \tag{7}$$

where A, B, and C are constants. The equivalent damping coefficient, b_{eqc}, is assumed to be constant.

The mechanical dynamics for the left dynamic crank length system, referred to here with the subscript *l*, are modelled as:

$$\frac{d}{dt}\dot{\theta}_{ml} = \frac{1}{J_{eql}}\left(K_{tl}i_l - b_{eql}\dot{\theta}_{ml} - \frac{1}{N_s N_p}\left(F_{gl} - F_{cl}\right)\right) \tag{8}$$

where N_s and N_p are the screw and planetary drive transmission ratios respectively, F_{gl} is a load due to gravity, and F_{cl} is a centrifugal force. The gravity term includes the component of the weight that acts parallel to the axis of the screw, as well as the friction in the linear guides, and is modelled as

$$F_{gl} = m_p g\left(\sin(\phi) + \mu\ \mathrm{sgn}\left(\dot{\theta}_{ml}\right)|\cos(\phi)|\right) \tag{9}$$

where μ is a coefficient of friction, and where the sgn term is used to ensure that the friction always opposes the direction of motion. The centrifugal force term accounts for the rotation of the crank as its length changes, and is modelled as

$$F_{cl} = m_p l_{cl}\dot{\phi}^2 \tag{10}$$

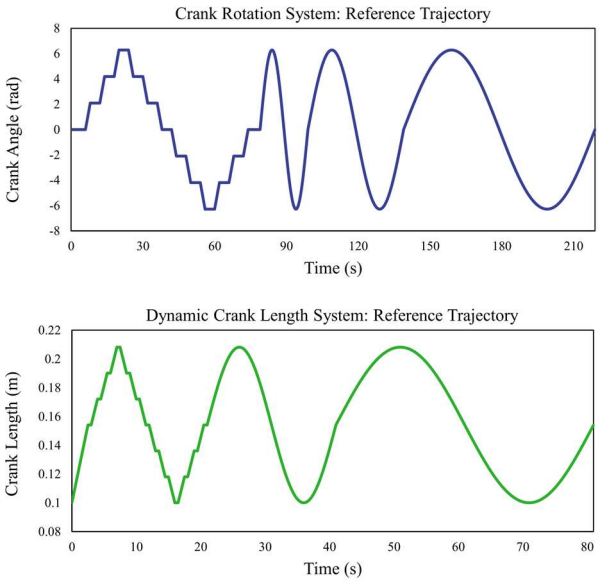


Figure 5. Reference trajectories used for the parameter estimation tests.

The state-space models presented here contain eight unknown inertia, damping, and friction parameters: A, B, and C for the variable equivalent inertia reflected to the central motor; the constant equivalent inertia referred to the crank length adjustment motor, J_{eql}; the mass of the pedal assembly, m_p; the coefficient of the equivalent damping at each motor, b_{eqc} and b_{eql}; and the coefficient of friction in the screw drive, μ. The following section describes the methods used to estimate these parameters.

2.4 Parameter Estimation

The unknown parameters in the system model were estimated using an optimization approach that minimized the differences between the model's predicted output and the measured output of the physical system. The motor constants, resistances, and inductances were taken from the supplier datasheets, and the optimization process was used to estimate the inertia, damping, and friction parameters. The models take applied voltage as input and calculate resulting motor position as output.

A sequence of physical tests were performed to collect data for this parameter estimation process. The system is unsuitable for stable open-loop operation, so closed-loop control was required for these tests. The optimal controller gains depend on the unknown parameters, so these tests used current and speed gains derived via the autotune feature of each motor controller, and the position loop gains were set manually. The tracking performance of the controller was not important for these tests because only the input voltage to each motor and the resulting position are required; as long as the system response was stable, the results are usable for the parameter estimation study. A reference motor position trajectory was provided to the controller for each test. The trajectories used for the tests are shown in Fig. 5, consisting of trapezoidal and sinusoidal signals. The trapezoidal sections tested linearity and repeatability, while the sinusoidal sections measured the response to varying frequencies [22]. Voltage data applied to the motor were obtained from the driver circuit, and position data were measured from the system's encoder.

The optimization process used the prediction error method [23]. The difference between the model's predicted output and the actual measured output is the error e_k, and the optimization algorithm attempts to minimize the objective function J_k [24]

$$e_k(t) = \theta_k(t) - \bar{\theta}_k(t) \tag{11}$$

$$J_k(t) = \frac{1}{N}\sum_{k=1}^{N} e_k(t)e_k(t)^T \tag{12}$$

where θ_k represents the measured motor position data and $\bar{\theta}_k$ represents the model outputs.

The bees algorithm was used to optimize the unknown parameters. This is a population-based search procedure inspired by the foraging behaviour of honeybees [25]. The algorithm was selected as appropriate to this problem because it does not rely on calculation of gradients, which would be problematic due to discontinuities in the state space models presented in the previous section. The bees algorithm initializes with a population of candidate solutions, analogous to scout bees exploring the environment. A subset of these solutions, deemed the most promising or "elite" sites, is selected for more intensive investigation. The algorithm then conducts a localized, intensive search around each of these elite sites by recruiting a larger number of agents to explore their immediate vicinity. A less intensive search is performed around other non-elite sites. This dual-pronged approach aims to achieve a balance between focused exploitation of high-quality regions and broader exploration of the search space.

In each iterative cycle of the algorithm, the population is updated by retaining the best-performing solutions discovered from the localized searches. The remaining population positions are replaced with new randomly-generated agents in unexplored areas of the search space. This scouting mechanism aims to prevent the search from converging prematurely on local optima. If implemented correctly, this iterative processes of local exploitation and random exploration converges toward a globally optimal or near-optimal solution.

Reasonable initial candidates for the inertia parameters were identified based on a combination of part specifications, CAD file data, basic mass moment of inertia definitions, and the parallel axis theorem. The initial candidates for damping and friction parameters were randomly generated. Algorithm parameters were based on the values used in similar studies [26-28], in which the population number varies between 20 and 100. To reduce the computational cost and shorten the optimization time, a population number of 40 was selected for this study. In each iteration, 12 promising sites and 4 elite sites were selected. The number of agents recruited to search near each elite site was 40, and the number recruited to search each non-elite promising site was 20. The number of iterations was set to 40.

Since the length of each crank is a variable in the model of the crank rotation system, test data were collected for six different crank length conditions. Each condition involved a different combination of left and right crank lengths, including one condition where both crank lengths varied following a triangle waveform (see Fig. 6a). The crank rotation system model parameters were fit to the data from the test in which both cranks were fixed at their minimum length. Using the resulting fitted parameters, the normalized root mean square error (NRMSE) between the model and the test data was calculated for all of the test conditions. Similarly, the dynamic crank length system model includes a term representing the crank rotation speed, so tests were repeated at three crank rotation speeds; the model parameters were fit to the data from a test at 10 rpm, and again the NRMSE was calculated for all test conditions. The mass term m_p appears in both models; since it has a larger influence in the dynamic crank length model, it was optimized for that model and treated as a constant in the central motor model.

2.5 Controller Parameters

Having estimated the inertial and dissipative parameters of the state-space models, they were then incorporated into MATLAB Simulink models of each system's control architecture as represented in Fig. 3, with the appropriate state-space equations in the "System" block. The PI controllers for each loop were synthesized using the MATLAB Closed-Loop PID Autotuner. This utility injects test signals into the simulated plant to estimate the frequency response, and optimizes the control parameters to meet the specified target bandwidths. The autotuning process was performed in two distinct stages:

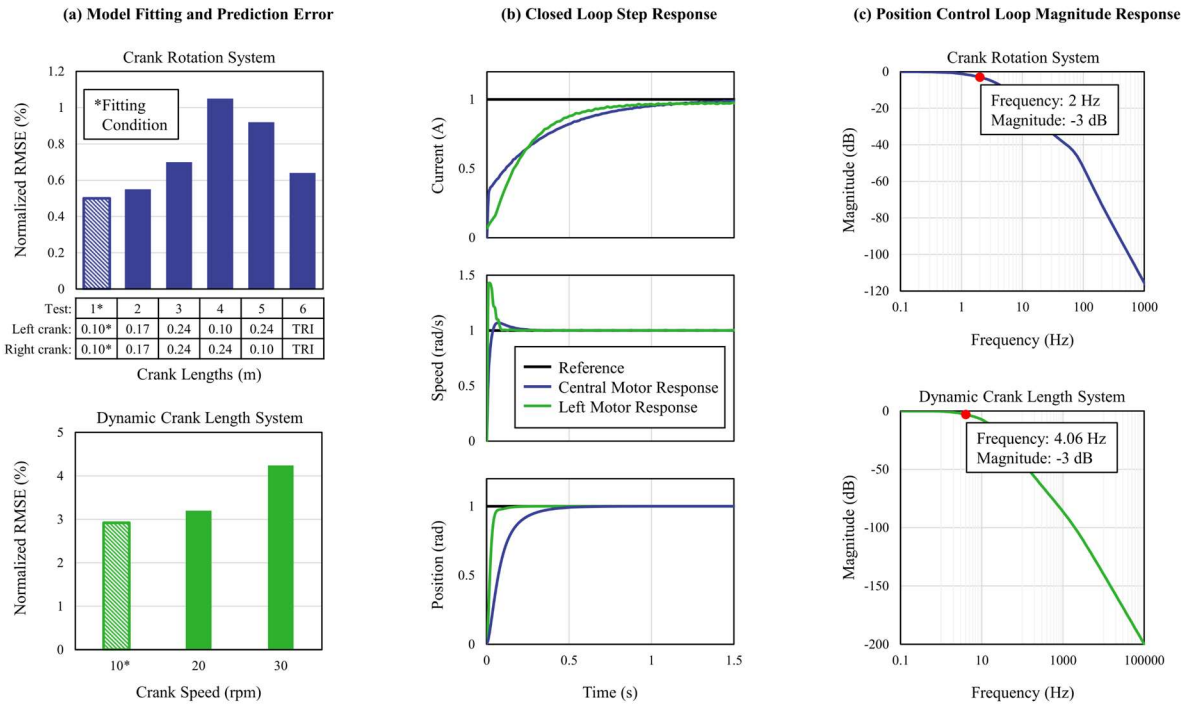


Figure 6. (a) Model fitting and prediction errors. The bars with hatched lines indicate the fitting errors, and the solid bars are the prediction errors. "TRI" indicates a test in which the crank lengths followed a triangle waveform. **(b)** The response of each loop in the cascade control architecture to a step command. **(c)** The magnitude response for each subsystem, with the bandwidth labelled.

First, the tool injected a small-amplitude, frequency-swept excitation signal (sinusoidal perturbation) into the closed-loop system model. The autotuner then measured the system's output response relative to this perturbation to estimate the frequency response near the desired bandwidth frequency. Subsequently, the algorithm optimized the proportional and integral gains to maximize the phase margin. To maintain stability within the cascade architecture, the loops were tuned sequentially from the inside out: beginning with the current loop (highest bandwidth), followed by the speed loop, and concluding with the position loop (lowest bandwidth). The resulting PI controllers were implemented in the physical system's LabVIEW control software.

The parameter estimation and controller tuning considered each HaCT subsystem independently. To evaluate both the performance of the tuned controllers and the fidelity of the developed models for the complete system, a trajectory tracking experiment was conducted. A reference pedal trajectory was commanded to both the physical system and the Simulink model. The actual motor positions were measured and the model's predicted response was recorded. The resulting data was used to quantify two error metrics: the tracking error, defined as the difference between the reference trajectory and the physical system's actual position; and the prediction error, defined as the difference between the physical device's measured position and the model's predicted position.

3 Results

3.1 Parameter Estimation Results

The optimization studies resulted in the estimated parameter values listed in Table 1. Based on these results, the equivalent inertia reflected to the central motor in the model varies from 2.1×10^{-4} kg·m^2 to 4.8×10^{-4} kg·m^2 as a function of the crank lengths. All estimated inertia terms are almost identical to the preliminary manual estimates. The estimated friction coefficient for the dynamic crank length system exceeds typical values for rolling contact, while the estimated equivalent

Table 1. Parameter estimation results

Subsystem	Parameter	Optimized value	
Crank rotation system	A	1.02×10^{-3}	kg
	B	3.21×10^{-4}	kg·m
	C	2.1×10^{-4}	kg·m^2
	b_{eqc}	1.8×10^{-3}	kg/s
Dynamic crank length system	J_{eql}	7.25×10^{-6}	kg·m^2
	b_{eql}	5.7×10^{-5}	kg/s
	m_p	4.77	kg
	μ	0.15	

Table 2. Tuned proportional and integral gains

System	Parameter	Current	Speed	Position
Crank Rotation System	K_p	0.1	0.4	15
	K_i	32	4.8	-
Crank Length System	K_p	0.1	0.1	24
	K_i	74	3.9	-

viscous damping coefficient is relatively low. This combination may reflect parameter compensation, wherein the optimization algorithm distributes dissipative effects between the two terms in a manner that is not strictly physical.

The model fitting and prediction errors corresponding to these parameters are shown in Fig. 6a. For the crank rotation system, the Normalized RMSE values are consistently low (~1%) across all validation tests, demonstrating good predictive accuracy for the investigated operating envelop. Since the validation tests encompass both sinusoidal and trapezoidal motion profiles, and represent distinct loading conditions achieved through crank length variation, which alters the mass distribution about the rotational axis, we can be confident that the model and its parameters are appropriate. The largest errors are observed when the left and right crank lengths are asymmetric (tests 4 and 5 in the plot), suggesting that the gravity torque term (Equation 6) does not fully capture the effects of asymmetry. That the error magnitude varies depending on which crank is longer suggests that the cranks are not perfectly identical as assumed; however, the effect of this discrepancy is negligible.

For the dynamic crank length system, the model fitting and validation errors are larger; this is to be expected since it is the more complex system. That the errors appear to scale with crank speed suggests that the centrifugal force term (Equation 10) does not fully capture its effects on the system. However, the observed Normalized RMSE values are still low (<5%) and are considered acceptable here.

3.2 Controller Parameter Results

Using the parameter estimates from the previous section, the controller gains for each subsystem were tuned as described above. The resulting proportional (K_p) and integral (K_i) parameters are listed in Table 2, and Fig. 6b illustrates the closed-loop step responses corresponding to these parameters. Figure 6c presents the magnitude response of the position control loop for each system, confirming that the system achieves the target bandwidths as specified in the design criteria (2 Hz and 4 Hz respectively). The results indicate that position control is achieved for both systems with no overshoot or steady-state

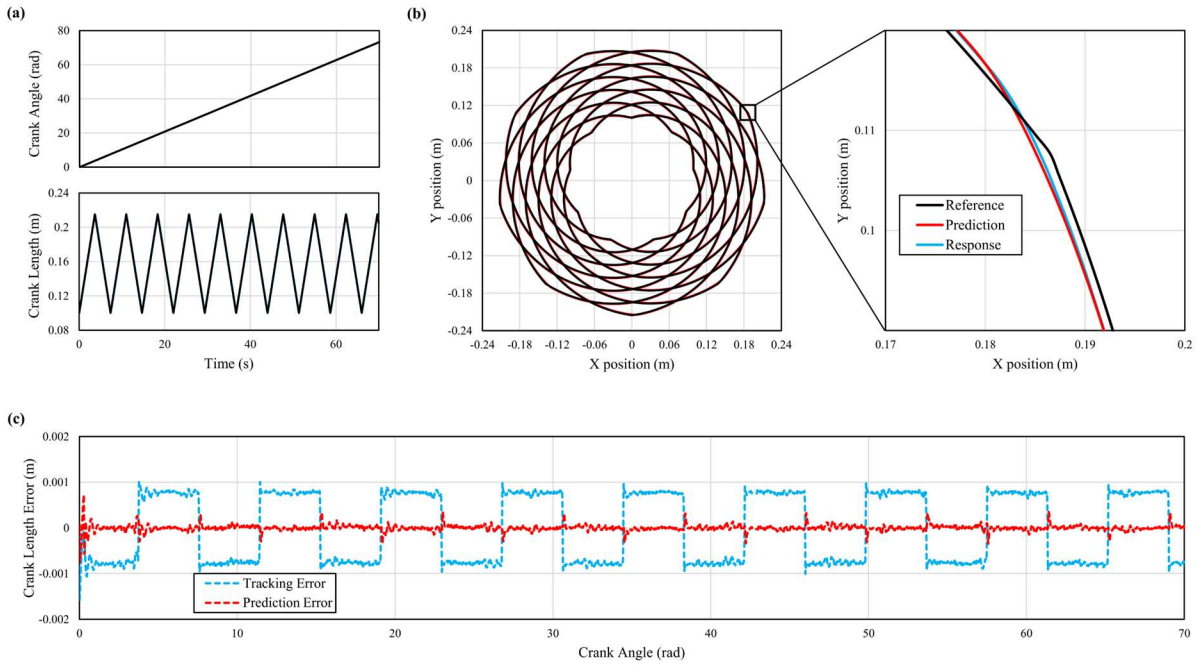


Figure 7. Complete system evaluation results. **(a)** The crank angle and crank length vs time. **(b)** The two-dimensional pedal trajectory followed during the test, with a magnified detail illustrating the reference, response, and predicted trajectories. **(c)** The tracking error (difference between reference and response) and prediction error (difference between prediction and response) plotted against crank angle.

error. In both subsystems, the current control loop response reaches the reference value gradually. Because the brushless DC motors in this system have high starting currents, the controller was specifically designed to prevent instantaneous current spikes that could damage the electronics. A controlled amount of overshoot is permitted within both speed loops. This design choice allows the system to respond more dynamically to rapid trajectory changes. These inner PI loops effectively eliminate steady-state error, so the integral term in the outer-loop position PI controller becomes redundant. Consequently, the position loops for both subsystems were reduced to purely proportional controllers as seen in Table 2. With these outer loop proportional gains, the system decelerates smoothly as it approaches the target angle, effectively balancing response speed with the necessity of preventing any position overshoot.

3.3 Complete System Demonstration Results

Thus far, the results have focused on each subsystem independently. To evaluate the overall system model and control strategy, a reference pedal trajectory was designed to emulate an expected use case of the device. This involved the cranks rotating at a constant speed while the length of each crank varied in a triangle waveform (Fig. 7a). The resulting two-dimensional trajectory of each pedal is shown in Fig. 7b. The system response predicted by the Simulink model is plotted along with the actual response of the physical system. The tracking error plot (Fig. 7c) indicates that there is a consistent lag of approximately 1 mm between the reference and the system response: while the crank length is increasing, the physical crank is consistently shorter than the reference, and vice versa when the crank length is decreasing. For this application, an error of ±1 mm is essentially undetectable; the typical variations in a user's ankle angle while cycling will have a much larger effect on the limb kinematics. The prediction errors are even smaller, and indicate that the complete closed-loop Simulink model of the system is a robust prediction tool.

4 Conclusion

The Haptic Cycling Trainer was designed to enable lower limb rehabilitation studies that combine elements of robot-assisted gait rehabilitation and cycling therapy. To achieve this, the system must be capable of dynamically changing the length of each crank independently while also controlling the rotation of the crank. The control system presented here is capable of following a desired foot trajectory within an acceptable margin of error for the intended application. Future work using the HaCT will investigate human motor adaptation in response to foot trajectories with clinical relevance, including human-in-the-loop optimization of trajectory parameters to elicit desired muscle activation patterns. The HaCT system model developed in this paper can accurately predict the system's response to command trajectories; this will support future studies on human-device interaction by enabling realistic representation of the mechatronic subsystems in *in silico* predictive neuromuscular modelling experiments.

References

1. Feigin, V.L., et al., *Global, regional, and national burden of stroke and its risk factors, 1990-2019: a systematic analysis for the Global Burden of Disease Study 2019.* Lancet Neurology, 2021. **20**(10): p. 795–820.
2. Jorgensen, H.S., et al., *Recovery of Walking Function in Stroke Patients - the Copenhagen Stroke Study.* Archives of Physical Medicine and Rehabilitation, 1995. **76**(1): p. 27–32.
3. Perry, J., et al., *Classification of Walking Handicap in the Stroke Population.* Stroke, 1995. **26**(6): p. 982–989.
4. Feigin, V.L., et al., *World Stroke Organization (WSO): Global Stroke Fact Sheet 2022.* Int J Stroke, 2022. **17**(1): p. 18–29.
5. Lord, S.E., et al., *Community ambulation after stroke: How important and obtainable is it and what measures appear predictive?* Archives of Physical Medicine and Rehabilitation, 2004. **85**(2): p. 234–239.
6. Pennycott, A., et al., *Towards more effective robotic gait training for stroke rehabilitation: a review.* Journal of Neuroengineering and Rehabilitation, 2012. **9**.
7. Baronchelli, F., et al., *The Effect of Robotic Assisted Gait Training With Lokomat® on Balance Control After Stroke: Systematic Review and Meta-Analysis.* Frontiers in Neurology, 2021. **12**.
8. van Asseldonk, E.H. and H. van der Kooij, *Robot-aided gait training with LOPES*, in *Neurorehabilitation Technology*. 2011, Springer. p. 379–396.
9. Høyer, E., A. Opheim, and V. Jørgensen, *Implementing the exoskeleton Ekso GTTM for gait rehabilitation in a stroke unit–feasibility, functional benefits and patient experiences.* Disability and Rehabilitation: Assistive Technology, 2022. **17**(4): p. 473–479.
10. Mehrholz, J., et al., *Electromechanical-assisted training for walking after stroke.* Cochrane Database of Systematic Reviews, 2020(10).
11. Krakauer, J.W., et al., *Getting Neurorehabilitation Right: What Can Be Learned From Animal Models?* Neurorehabilitation and Neural Repair, 2012. **26**(8): p. 923–931.
12. Vanroy, C., et al., *Effectiveness of Active Cycling in Subacute Stroke Rehabilitation: A Randomized Controlled Trial.* Archives of Physical Medicine and Rehabilitation, 2017. **98**(8): p. 1576–1585.
13. Sancetta, S.M. and R.J. Carleton Jr, *Variable resistance bicycle ergometer for performance of recumbent exercise.* Review of Scientific Instruments, 1957. **28**(2): p. 125–126.
14. Elmer, S.J. and J.C. Martin, *Construction of an isokinetic eccentric cycle ergometer for research and training.* J Appl Biomech, 2013. **29**(4): p. 490–5.
15. Walsh, J.A., et al., *A Semi-recumbent Eccentric Cycle Ergometer Instrumented to Isolate Lower Limb Muscle Contractions to the Appropriate Phase of the Pedal Cycle.* Front Physiol, 2021. **12**: p. 756805.
16. Walsh, J.A., et al., *Global Corticospinal Excitability as Assessed in A Non-Exercised Upper Limb Muscle Compared Between Concentric and Eccentric Modes of Leg Cycling.* Sci Rep, 2019. **9**(1): p. 19212.

17. Dawson-Elli, A.R. and P.G. Adamczyk, *Design and Validation of a Lower-Limb Haptic Rehabilitation Robot.* IEEE Trans Neural Syst Rehabil Eng, 2020. **28**(7): p. 1584–1594.
18. Du, Z., et al., *Design of PI Controller for a Class of Discrete Cascade Control Systems.* Ieee Transactions on Automation Science and Engineering, 2023. **20**(4): p. 2607–2615.
19. Zhang, H., et al., *High-Dynamic and Low-Cost Sensorless Control Method of High-Speed Brushless DC Motor.* Ieee Transactions on Industrial Informatics, 2023. **19**(4): p. 5576–5584.
20. Karapinar, U., et al., *Cascaded Controller Algorithm Design for a Brushless DC Motor with Matlab/Simulink and MCU Implementation.* 2013 21st Signal Processing and Communications Applications Conference (SIU), 2013.
21. Kudzia, P., S.N. Robinovich, and J.M. Donelan, *Characterizing the performance of human leg external force control.* Sci Rep, 2022. **12**(1): p. 4935.
22. Zhu, Y., *Multivariable system identification for process control*. 2001: Elsevier.
23. Dao, T. and C. Chen, *A study of bicycle dynamics via system identification approaches.* Journal of the Chinese Institute of Engineers, 2012. **35**(7): p. 853–868.
24. Brunot, M., et al., *A Separable Prediction Error Method for Robot Identification.* Ifac Papersonline, 2016. **49**(21): p. 487–492.
25. Sahin, M. and Z. Kulunk, *Optimization of spring parameters by using the Bees algorithm for the foldable wing mechanism.* Scientific Reports, 2022. **12**(1).
26. Satpathy, A., et al., *Green Vehicle Routing Optimisation Using the Bees Algorithm*, in *Intelligent Engineering Optimisation with the Bees Algorithm*. 2024, Springer. p. 317–339.
27. Moradi, S., P. Razi, and L. Fatahi, *On the application of bees algorithm to the problem of crack detection of beam-type structures.* Computers & Structures, 2011. **89**(23-24): p. 2169–2175.
28. Pham, D. and M. Castellani, *A comparative study of the Bees Algorithm as a tool for function optimisation.* Cogent Engineering, 2015. **2**(1).